Early Results from GLASS-JWST. VI. Extreme Rest-optical Equivalent Widths Detected in NIRISS Wide Field Slitless Spectroscopy

K. Boyett[1,2] , S. Mascia[3] , L. Pentericci[3] , N. Leethochawalit[1,2,4] , M. Trenti[1,2] , G. Brammer[5,6] , G. Roberts-Borsani[7] ,
V. Strait[5,6] , T. Treu[7] , M. Bradac[8,9] , K. Glazebrook[10] , A. Acebron[11,12] , P. Bergamini[11,13] , A. Calabrò[3] ,
M. Castellano[3] , A. Fontana[3] , C. Grillo[11,12] , A. Henry[14,15] , T. Jones[9] , D. Marchesini[16] , C. Mason[5,6] ,
A. Mercurio[17] , T. Morishita[18] , T. Nanayakkara[10] , P. Rosati[19] , C. Scarlata[20] , E. Vanzella[13] , B. Vulcani[21] ,
X. Wang[18] , and C. Willott[22]

[1] School of Physics, University of Melbourne, Parkville 3010, VIC, Australia; kit.boyett@unimelb.edu.au
[2] ARC Centre of Excellence for All Sky Astrophysics in 3 Dimensions (ASTRO 3D), Australia
[3] INAF Osservatorio Astronomico di Roma, Via Frascati 33, I-00078 Monteporzio Catone, Rome, Italy
[4] National Astronomical Research Institute of Thailand (NARIT), Mae Rim, Chiang Mai, 50180, Thailand
[5] Cosmic Dawn Center (DAWN), Denmark
[6] Niels Bohr Institute, University of Copenhagen, Jagtvej 128, DK-2200 Copenhagen N, Denmark
[7] Department of Physics and Astronomy, University of California, Los Angeles, 430 Portola Plaza, Los Angeles, CA 90095, USA
[8] University of Ljubljana, Department of Mathematics and Physics, Jadranska ulica 19, SI-1000 Ljubljana, Slovenia
[9] Department of Physics and Astronomy, University of California Davis, 1 Shields Avenue, Davis, CA 95616, USA
[10] Centre for Astrophysics and Supercomputing, Swinburne University of Technology, P.O. Box 218, Hawthorn, VIC 3122, Australia
[11] Dipartimento di Fisica, Università degli Studi di Milano, Via Celoria 16, I-20133 Milano, Italy
[12] INAF - IASF Milano, Via A. Corti 12, I-20133 Milano, Italy
[13] INAF - OAS, Osservatorio di Astrofisica e Scienza dello Spazio di Bologna, Via Gobetti 93/3, I-40129 Bologna, Italy
[14] Space Telescope Science Institute, 3700 San Martin Drive, Baltimore, MD 21218, USA
[15] Center for Astrophysical Sciences, Department of Physics & Astronomy, Johns Hopkins University, Baltimore, MD 21218, USA
[16] Department of Physics and Astronomy, Tufts University, 574 Boston Avenue, Medford, MA 02155, USA
[17] INAF—Osservatorio Astronomico di Capodimonte, Via Moiariello 16, I-80131 Napoli, Italy
[18] Infrared Processing and Analysis Center, Caltech, 1200 E. California Blvd., Pasadena, CA 91125, USA
[19] Dipartimento di Fisica e Scienze della Terra, Università degli Studi di Ferrara, Via Saragat 1, I-44122 Ferrara, Italy
[20] School of Physics and Astronomy, University of Minnesota, Minneapolis, MN 55455, USA
[21] INAF Osservatorio Astronomico di Padova, vicolo dell'Osservatorio 5, I-35122 Padova, Italy
[22] NRC Herzberg, 5071 West Saanich Rd., Victoria, BC V9E 2E7, Canada

Abstract

Wide Field Slitless Spectroscopy (WFSS) provides a powerful tool for detecting strong line emission in star-forming galaxies (SFGs) without the need for target preselection. As part of the GLASS-JWST Early Release Science (ERS) program, we leverage the near-infrared wavelength capabilities of NIRISS (1–2.2 μm) to observe rest-optical emission lines out to $z \sim 3.4$, to a depth and with a spatial resolution higher than ever before (Hα to $z < 2.4$; [O III]+Hβ to $z < 3.4$). In this Letter we constrain the rest-frame [O III]λ5007 equivalent width (EW) distribution for a sample of 76 $1 < z < 3.4$ SFGs in the A2744 Hubble Frontier Field and determine an abundance fraction of extreme emission line galaxies with EW > 750Å in our sample to be 12%. We determine a strong correlation between the measured Hβ and [O III]λ5007 EWs, supporting that the high [O III]λ5007 EW objects require massive stars in young stellar populations to generate the high-energy photons needed to doubly ionize oxygen. We extracted spectra for objects up to 2 mag fainter in the near-infrared than previous WFSS studies with the Hubble Space Telescope. Thus, this work clearly highlights the potential of JWST/NIRISS to provide high-quality WFSS data sets in crowded cluster environments.

Unified Astronomy Thesaurus concepts: Starburst galaxies (1570); Emission line galaxies (459); James Webb Space Telescope (2291)

1. Introduction

The study of star-forming galaxies (SFGs) has benefited from the development of the Hubble Space Telescope (HST) Wide Field Camera 3 (WFC3) Wide Field Slitless Spectroscopy (WFSS), where the low background of space-based observatories provides sensitivity to the dispersed light of sources through a low-spectral resolution grism ($R = \frac{\lambda}{\Delta\lambda} \sim 100$–200). The advantage compared to fixed-slit or multiobject

spectroscopy is the ability to obtain spectra for every object in the field of view (FOV) without the need for preselection and without being encumbered by slit losses. Substantial work using WFSS on HST/WFC3 over the past decade, especially from survey programs such as GLASS (Schmidt et al. 2014; Treu et al. 2015), WISPS (Atek et al. 2010; Bagley et al. 2020), and 3D-HST (Momcheva et al. 2016), has seen the detection of line emission for large galaxy samples over a wide redshift range. With the advent of the James Webb Space Telescope (JWST) and NIRISS (Doyon et al. 2012; Willott et al. 2022), the observable spectral range available to WFSS now extends further into the near-infrared. The additional wavelength range now allows key emission lines to be traced to higher redshifts. The JWST GLASS Early Release Science (ERS) program (ERS

1324, PI Treu; Treu et al. 2022) is one of the first and deepest extragalactic data sets of the ERS strategy, and as part of this program we obtain NIRISS/WFSS observations of the Hubble Frontier Field Abell 2744 (A2744, Lotz et al. 2017) to study the SFG population.

Through WFSS, it is possible to examine the equivalent widths (EWs) of rest-optical emission lines in SFGs, which can be used to understand the conditions of their interstellar medium (ISM) and the nature of their underlying stellar population. WFSS is well leveraged to identify galaxies with strong line emission, including those with weak stellar continua that may be too faint to enter broadband-magnitude selections. The combination of strong nebular line emission and weak rest-optical stellar continuum is characteristic of galaxies going through an upturn/burst of star formation with a young stellar population. The UV emission from the massive short-lived O/B-type stars powers the strong nebular lines and, without a dominant older stellar population providing a strong stellar continuum in the rest-optical, these galaxies exhibit large EWs (hereafter, extreme emission line galaxies or EELGs). Due to the young stellar population, the SFGs in this EELG phase produce enhanced ionization efficiencies and potentially larger escape fractions of UV ionization radiation than typical SFGs. This makes EELGs of special interest to astronomers, especially in terms of their potential UV-ionizing photon contribution during the epoch of reionization, and they have been studied spectroscopically both locally and at ($z < 3$) moderate redshifts (e.g., van der Wel et al. 2011; Atek et al. 2014; Amorin et al. 2015; Maseda et al. 2018; Tang et al. 2019), and at higher redshifts ($z > 5$) strong line emitters have been identified through measured flux excess in photometric surveys (e.g., Smit et al. 2014; Endsley et al. 2021).

In this Letter, we use the GLASS-ERS JWST/NIRISS observations of the A2744 to study the rest-optical emission line properties of SFGs at $1 < z < 3.4$ (where [O III] is observable). The A2744 region has been well studied and large samples of galaxies with spectroscopic redshifts at our desired epoch have been previously identified. We focus this early paper on the A2744 spectroscopic samples reported in Richard et al. (2021), Bergamini et al. (2022), and Treu et al. (2015). Therefore, these objects are the focus of this early work. In the future we will use the same data set to also search for emission line galaxies without previous redshift determination. In Section 2, we briefly introduce the JWST/NIRISS observations. In Section 3, we use NIRISS/WFSS to measure the rest-optical line emission ([O II], Hβ, [O III], and Hα) from which we determine the EWs of these SFGs in Section 4. Finally, we discuss the most extreme line emitters, EELGs, in Section 5.

We note that since the NIRISS FOV is centered on the A2744 cluster, all objects in our sample will be subject to some degree of magnification due to gravitational lensing; however, in this study we only consider relative quantities for each target (EWs). Therefore our results are independent of magnification, yet gravitational lensing allows us to study fainter galaxies at higher spatial resolution. We refer the reader to Roberts-Borsani et al. (2022, Paper I of this series) and Vanzella et al. (2022, Paper VII of this series) for GLASS-ERS studies that provide detailed discussion and utilization of gravitational lensing. In this study we only measure integrated line properties of galaxies and we refer the reader to Wang et al. (2022, Paper IV of this series) for a GLASS-ERS study of

spatially resolved emission line properties. Where applicable, we use $H_0 = 70$ km s^{-1} Mpc^{-1}, $\Omega_m = 0.3$, and $\Omega_\wedge = 0.7$. All magnitudes are in the AB system (Oke and Gunn 1983).

2. JWST/NIRISS Imaging and Spectroscopy of HFF A2744

As part of the GLASS-ERS strategy, we use the WFSS mode of the JWST/NIRISS instrument to conduct 1.0–2.2 μm low-resolution spectroscopy (average spectral resolution of $R \sim 150$) over the A2744 region. The NIRISS component of the GLASS-ERS survey utilizes a single pointing centered on the core of the A2744 cluster,[23] giving a full area of $2.2' \times 2.2'$. The WFSS observations and associated direct imaging are obtained using the F115W, F150W, and F200W blocking filters. For the full details of the GLASS-ERS data acquisition, observing strategy, and data reduction we refer the reader to Treu et al. (2022) and Roberts-Borsani et al. (2022).

At this early stage of the mission, there is ongoing development of JWST calibration files and pipelines, which means the quality of the extracted data will likely improve over time. The results in this paper are based on a NIRISS data reduction that utilized the following pedigree of data products: `CAL_VER`=1.5.2, `CRDS_VER`=11.13.1, and `CRDS_CTX`=jwst_0881.pmap. The EW measurements we present in this Letter are wavelength-independent relative quantities (ratio of line flux to continuum flux density at the same wavelength) and therefore should be relatively unaffected by future changes to the calibration files.

3. NIRISS Detection of Rest-optical Emission Lines in Individual Sources

In this Letter, we will focus on NIRISS detections of rest-optical emission lines in a sample of galaxies that have existing spectroscopic redshifts measurements (based on the detection of rest-UV/optical lines) in the range $1 < z < 3.4$, where the [O III] doublet falls within the NIRISS wavelength coverage. This robust sample is collated from several ancillary studies of the A2744 region, utilizing both ground-based rest-UV MUSE spectroscopy (Richard et al. 2021; Bergamini et al. 2022, 86 objects), and space-based rest-optical HST/WFC3 WFSS from Treu et al. (2015, 15 objects). There are 101 spectroscopic candidates within our FOV in our desired redshift range, although we note that five may be less robust due to quality flags that mark their redshift as "uncertain" (Bergamini et al. 2022) or "tentative/possible" (Treu et al. 2015; Richard et al. 2021).

Our sample represents only a subset of all the emission line galaxies observed with NIRISS and the selection of objects with existing spectroscopic redshifts, where previous redshift determination was reliant on line detection, may bias our sample against weak line emitters or heavily absorbed objects (which would be too reddened and faint to exhibit strong rest-UV emission lines). For example, there may be a population of Hα emitters with no UV counterpart that is missed by this preselection. Consideration of the selection effects and an analysis with a full statistical sample is beyond the scope of this Letter and will be performed in the future. Instead, here we focus on the robust sample as a demonstration of the capabilities of JWST/NIRISS.

We utilize the grism redshift and line analysis tool (`Grizli`;[24] Brammer & Matharu 2021) to extract and model the grism spectra associated with each of our targets (see

---

[23] Cluster coordinates (J2000) R.A. 00:14:23.4, decl. −30:23:26.
[24] https://github.com/gbrammer/grizli

Roberts-Borsani et al. 2022 for further details). For 16 objects (all selected from rest-UV spectroscopy), we found no coordinate matches within $1''$ in the segmentation map of the composite NIRISS F115W+F150W+F200W direct image and we remove these from our analysis. From visual inspection of these 16 targets, 7 show no evidence of continuum emission in the direct images at the reported catalog coordinates and are either examples of extremely blue objects with negligible emission at long wavelength, or more likely, that these sources are not genuine. The latter is supported by each of these seven having low-reliability quality flags in the Richard et al. (2021) input catalog. Visual inspection of the remaining nine objects reveals each to be a faint-diffuse source near a bright foreground galaxy. In each case the Grizli source extraction has been limited by the significant contamination from the neighbor. We do not attempt to force the extraction of these nine, due to the significant contamination of their dispersed light in both of the orthogonal PRISM images.

From the 85 matched objects with extracted spectra, we perform the Grizli modeling twice, first with a broad $(0.5 < z < 5.0)$ redshift fitting range and again with a narrow $(\Delta z \pm 0.1)$ redshift fitting range centered on either the resultant Grizli redshift or the existing spectroscopic redshift if no lines are detected with NIRISS. The first run is used to identify cases when alternative redshift solutions may be present due to new NIRISS line detections, and the second is to aid the identification of weaker lines by reducing the free parameters in the modeling once a confident redshift solution is found.

Within the 2.2×2.2 area, 76 of the 85 galaxies have a NIRISS ($> 5\sigma$) line detection. Of these, 54 have multiple NIRISS line detections. The uncertainty in the line flux reported by Grizli reflects instrumental effects and modeling procedure. We note that uncertainties on faint lines also reflect the presence of additional strong lines in the spectrum which can corroborate the redshift solution. Quoting a line flux limit for the entire survey is not feasible, as the flux limit depends on the level of contamination from nearby sources. Accordingly, we provide the observed median 5σ line flux limit, with associated 16th and 84th percentiles. We measure line flux limits of $1.5^{+1.9}_{-0.5} \times 10^{-17}$, $1.0^{+1.9}_{-0.4} \times 10^{-17}$ and $7.6^{+9.1}_{-3.1} \times 10^{-18}$ erg s^{-1} cm^{-2} for the F115W, F150W, and F200W filters respectively, using the stated calibration files (these are subject to change in line with calibration file updates).

From the initial run, 23 sources with detected line emission have a primary redshift solution that disagrees with the previous measurement. Upon inspection, we categorize these into three groups: we believe two objects[25] have previously misidentified redshifts based on the observed wavelengths of line emission detected with NIRISS and in the previous spectroscopy; seven objects have a close-probability secondary redshift solution from Grizli that agrees with the existing value and is supported by additional line detections in previous spectroscopy, and in the second run we utilize their secondary Grizli solution; finally 14 objects have solutions based on weak ($< 10\sigma$) detections of only one (7) or two (7) lines in NIRISS that can allow the redshift solution to remain ambiguous, and for these we rely on the existing spectroscopic redshift for the second run. The nine galaxies with no NIRISS line detection either have weak rest-optical line emission, lie at

alternative redshifts where no lines are present in our wavelength window, or have considerable contamination from the dispersed light from neighboring sources such that their lines are no longer detectable. We note that of the five galaxies with less robust redshift quality flags, three have their redshift confirmed, one is identified to lie at an alternative redshift and 1 had no line detections. This indicates that some of the targets without NIRISS detections may be due to the quality of the input spectroscopic redshifts. Finally, we inspect one object (NIRISS ID:1710) that had two different spectroscopic redshifts based on claimed [O II]-line detections from MUSE ($z = 1.2$) and HST/WFC3 WFSS ($z = 1.9$). From our detection of Hα and [O III] in NIRISS, we measure $z_{\rm NIRISS} = 1.16$ and propose that the HST line was actually the misidentified [O III] line.

In Figure 1 we present the 2D and 1D NIRISS spectra for three objects that demonstrate the capabilities of JWST/ NIRISS: ID 2314, which had the largest measured [O III]$\lambda 5007$ EW in our sample (determined in the next section); ID 683, which was the faintest source (F150W 29.1 ± 0.2 mag[26]) with a NIRISS line detection; and ID 2707, which shows significant detections in all rest-optical lines considered in this work. The distribution of Grizli-derived spectroscopic redshifts for galaxies with NIRISS line detections is shown in the top panel of Figure 2; redshifts are taken from the second Grizli modeling. In the bottom panel the previous spectroscopic redshifts and the Grizli-derived NIRISS redshifts are compared. Excellent agreement is found between the two spectroscopic redshift measurements, with NIRISS line detections confirming 87% (74/85) of the sample and only identifying two galaxies to be at alternative redshifts. We note a small $\sigma_{\rm NMAD}$[27] $= 0.003$ and only 14% (11/76) of those with line detections show notable deviation in spectroscopic redshift $(\Delta z / (1 + z_{\rm NIRISS}) > 5\sigma_{\rm NMAD})$.

In summary, we are able to recover accurate redshifts using NIRISS for nearly the entire sample, but note that visual inspection is required in a significant fraction of cases to clearly identify the emission lines. Nonetheless these are early results and the performance of automated redshift and line flux measurements is likely to improve with updated NIRISS calibration and contamination modeling.

4. Determination of Rest-optical Equivalent Widths

To determine individual EW, we start by measuring the integrated line fluxes for emission lines detected at $\geqslant 5\sigma$ in NIRISS/WFSS and place upper limits on those below this threshold. In this analysis, we only consider the 76 galaxies that have at least one NIRISS line detection and emission lines within the NIRISS wavelength range. For the objects in the field with NIRISS-detected line emission (66/76 have [O III] detections), we determine the EW as the ratio of the line flux to the continuum flux density (at the wavelength of the line) where both quantities are "total" values.

---

[25] NIRISS ID:2808 and 1911. These NIRISS IDs refer to the provided machine-readable table, which contains the rest-optical properties and coordinates.
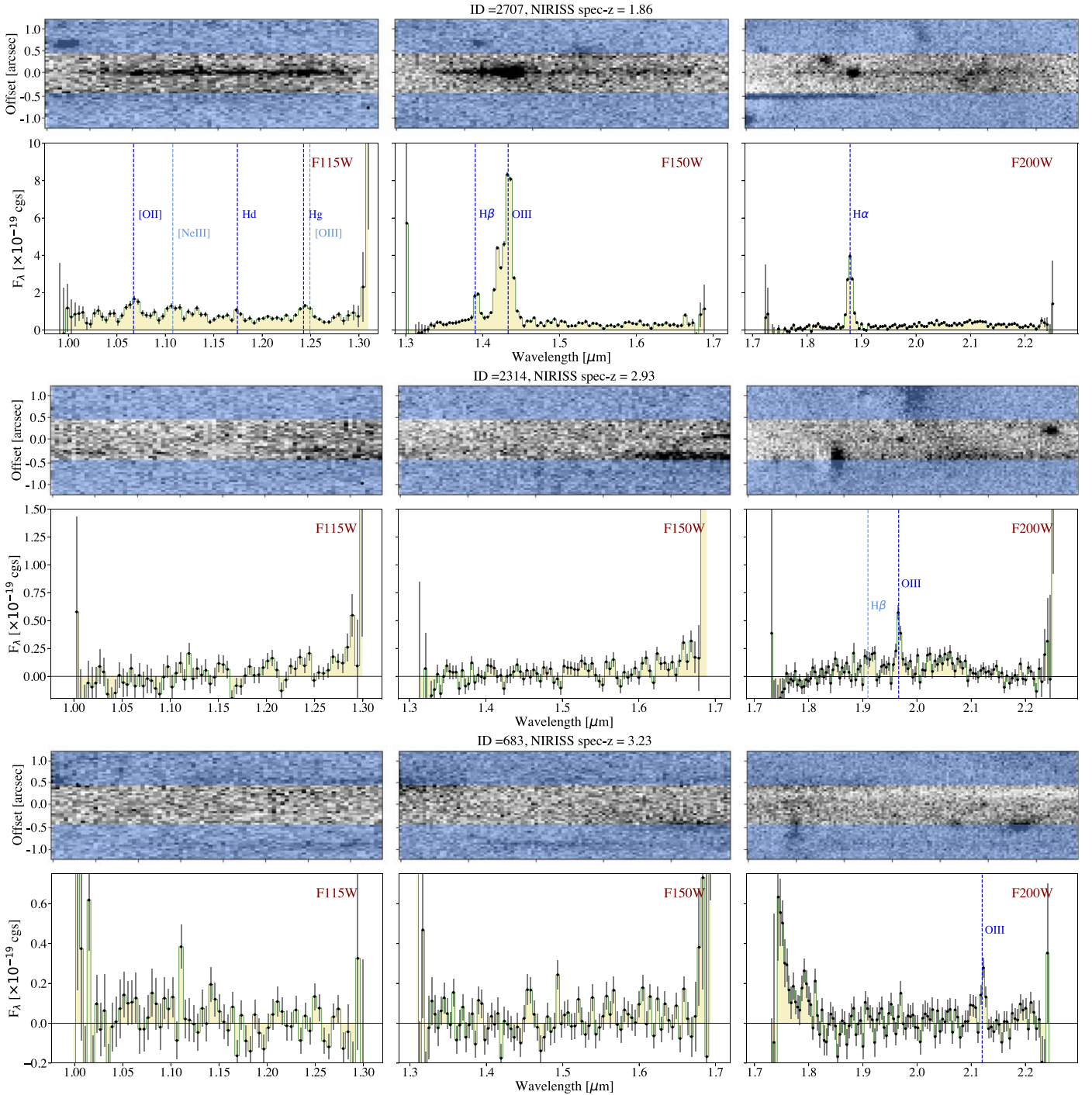
[26] We note a consistent magnitude offset is observed between the NIRISS F150W total magnitudes and the associated HST F160W total magnitudes (F160W - F150W = $+0.5 \pm 0.1$ mag) for the sources from Bergamini et al. (2022). We apply this offset correction to the quoted magnitude. This discrepancy is likely to be automatically solved once updated NIRISS in-orbit calibration data become available.

[27] $\sigma_{\rm NMAD}$ as defined by Brammer et al. (2008). $\sigma_{\rm NMAD} = 1.48 \times$ median($|\Delta z - {\rm median}(\Delta z)|/(1 + z_{\rm NIRISS})$), where $\Delta z = z_{\rm NIRISS} - z_{\rm INPUT}$.

Figure 1. NIRISS/WFSS `Grizli`-extracted 2D and 1D spectra for three example galaxies in our sample with large [O III]λ5007 EWs (these measurements are described in Section 3), to first demonstrate the typical high-quality spectra and then to show how far we can push the NIRISS data. In the 1D panels we mark the location of ⩾5σ (dark blue) and ⩾3σ (light blue) detected emission lines. Top: a galaxy with strong detections in each rest-optical emission line; ID 2707 ($z = 1.82$) with a rest-frame [O III]λ5007 EW = 1003 ± 37 Å. The quality of these NIRISS spectra also allows the detection of weaker rest-optical lines including Ne III]λ3869], Hδ, and the blended Hγ+[O III]λ4363. Middle: the galaxy in our full sample with the largest EW; ID 2314 ($z = 2.93$) with a rest-frame [O III]λ5007 EW = 1901 ± 787 Å. Here the EW signal-to-noise is <5, although we note both the line and broadband continuum are detected above this threshold. Bottom: the faintest galaxy (F150W total mag = 29.1 ± 0.2) in our full sample with a [O III]λ5007 EW measurement; ID 683 ($z = 3.23$) with a rest-frame [O III]λ5007 EW = 446 ± 109 Å.

We choose to measure the continuum flux density from the broadband imaging rather than directly from the WFSS spectra. This is because the continuum sensitivity in the spectra and the contamination due to an overlap with other spectra can lead to large uncertainties on the measured EW for objects with faint continua.

Total line fluxes and their uncertainty are obtained from the `Grizli` extraction pipeline, along with broadband photometry for each source in the F115W, F150W, and F200W direct images. Photometric fluxes are obtained from a 0″36 diameter aperture with a total-aperture correction applied, and the spectral extraction from `Grizli` is based on the segmentation
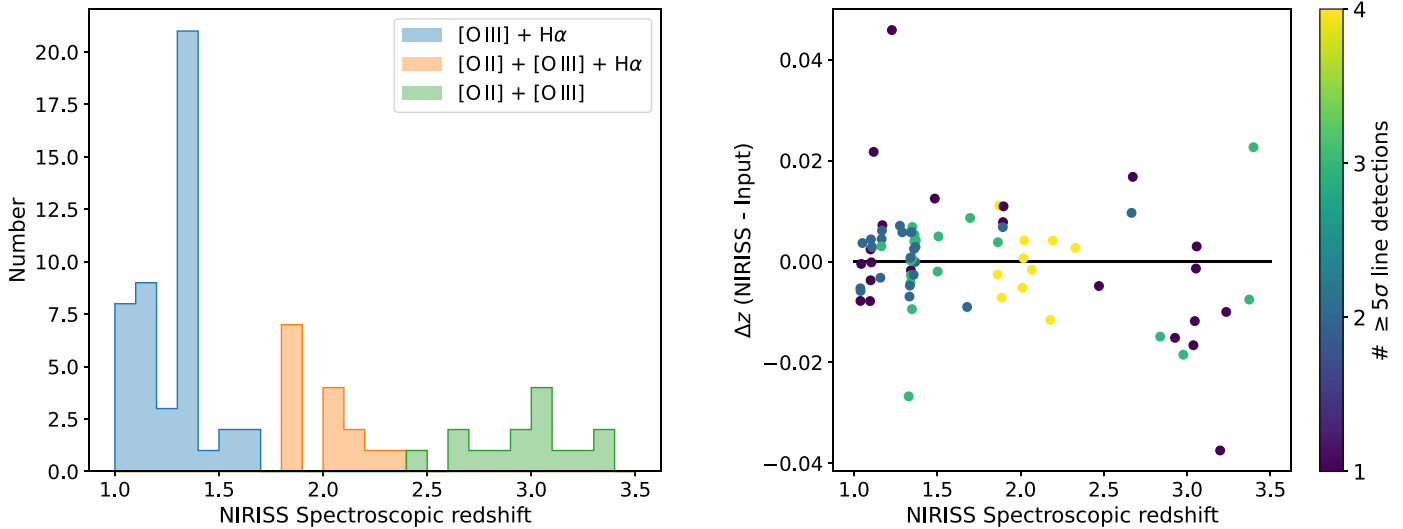
Figure 2. Left panel: the $1 < z < 3.4$ NIRISS spectroscopic redshift distribution of 76 galaxies with NIRISS detections ($>5\sigma$) of Hα, [O III], Hβ, or [O II]. The distribution is split into three colors based on the set of emission lines that are covered by the observations at different redshifts (e.g., [O II] is only visible at $z > 1.7$ and Hα at $z < 2.4$). We note an apparent overdensity of 21 independent galaxies in the range $1.33 < z < 1.37$. Right panel: the comparison of the NIRISS Grizli-derived and input spectroscopic redshifts, color coded by the number of $>5\sigma$ NIRISS line detections. Excellent agreement is found in the sample, with the majority of targets having their previous redshifts confirmed through multiple NIRISS line detections. Only two galaxies (NIRISS ID:2808 and 1911, $\Delta z > 0.5$) are found to have previously misidentified redshifts solutions.

map obtained from the direct images. Therefore, Grizli photometry and spectroscopy are obtained on a self-consistent aperture. Using the self-consistent continuum and emission line fluxes results in galaxy-integrated EW values.

To validate our approach of combining line fluxes from slitless spectroscopy with continuum flux densities from photometry, we select galaxies from the bright end of our sample, where the continuum emission can be constrained from the slitless spectroscopy and provide robust EW measurements from the spectra alone for comparison. We find good agreement in the EWs determined using broadband imaging and using slitless spectroscopy alone, i.e., the measurements agree within $\sim$0.1 dex (1σ) with a minor systematic bias of 0.06 dex for 16 objects with $21 < m_{AB} < 23$. We further note that the estimated fractional uncertainty associated with the direct measurement of the EW from the slitless spectroscopy alone is consistent with the broadband-derived method.

All galaxies for which we identify emission lines are well detected ($\geqslant 5\sigma$) in the associated imaging, and are thus suitable for EW measurements. The faintest source with a NIRISS detection has an F150W 29.1 ± 0.2 magnitude (compared to a sample median F150W magnitude of 24.57), consistent with the estimated 5σ magnitude limit for the preimaging (Treu et al. 2022). We assume a flat in f_ν continuum slope and subtract the flux contribution from any detected emission lines contributing to that filter. EWs are then taken as the ratio of the line flux to the continuum flux density, and are brought to the rest-frame using the NIRISS Grizli-derived redshift. The assumed continuum slope and the contribution of nondetected emission lines does not significantly affect the measured EW distribution (e.g., see Boyett et al. 2022).

When an emission line is not detected (10/76 do not have [O III] detections), we report a 5σ upper limit on the line flux using the modeled line uncertainty. The 5σ EW upper limit is then taken as the ratio of this flux limit and the continuum flux density at the expected location. Here, we rely on the spectroscopic redshift derived from other NIRISS-detected lines (Hα, Hβ, [O II]). We present the distribution of [O III]

λ5007 EWs in the $1 < z < 3.4$ sample in Figure 3, adopting a 1:3 flux ratio between the doublet. We observe a broad dynamic range of [O III]λ5007 EW spanning $\sim$10–2000 Å, with a clear peak at $\sim$150 Å. We note that our sample is likely incomplete at low EWs due to our line sensitivity and sample selection; we intend to revisit the completeness in future work. We note 14 objects with [O III] EW measurements are at $2.4 < z < 3.4$, an epoch previously unobtainable with WFSS on HST.

We additionally present the comparison of the EWs for Hβ and [O III]λ5007 for galaxies where both have $\geqslant 5\sigma$ measurements. We observe a clear positive correlation that is in agreement with the trend found by Sanders et al. (2020; MOSDEF, ground-based) for $z \sim 2.3$ SFGs and Tang et al. (2021b, 2022) for $z \sim 2$ SFGs, supporting the accuracy of our measurements. The NIRISS sensitivity provides us higher-precision EW measurements and we fit a linear function and report best-fit coefficients: $\log_{10}(\text{EW}_{\text{H}\beta}) = 0.88x - 0.39$, with $x = \log_{10}(\text{EW}_{[\text{O III}]\lambda5007})$, and measure a scatter of 0.16 dex. The [O III] and Hβ EW measurements are provided in Table 1 for the subset of objects where all rest-optical emission lines are observable and in a machine-readable format for the full data set.

5. Identification of Extreme Emission Line Galaxies with NIRISS WFSS

There is no strict EW threshold for what is considered an EELG, and within literature many studies introduce different EW thresholds and utilize different emission lines (Hβ, Hα, [O III]) in their selection (e.g., Atek et al. 2011; van der Wel et al. 2011; Amorin et al. 2015; Terlevich et al. 2015; Maseda et al. 2018; Tang et al. 2019; Du et al. 2020; Onodera et al. 2020). We adopt a rest-frame >750Å [O III]λ5007 EW criteria. This threshold is physically motivated by SFGs above this value being observed to exhibit larger ionizing photon production efficiencies than typical SFGs (e.g., Tang et al. 2019 at $z \sim 2$) and the potential for high escape fractions of
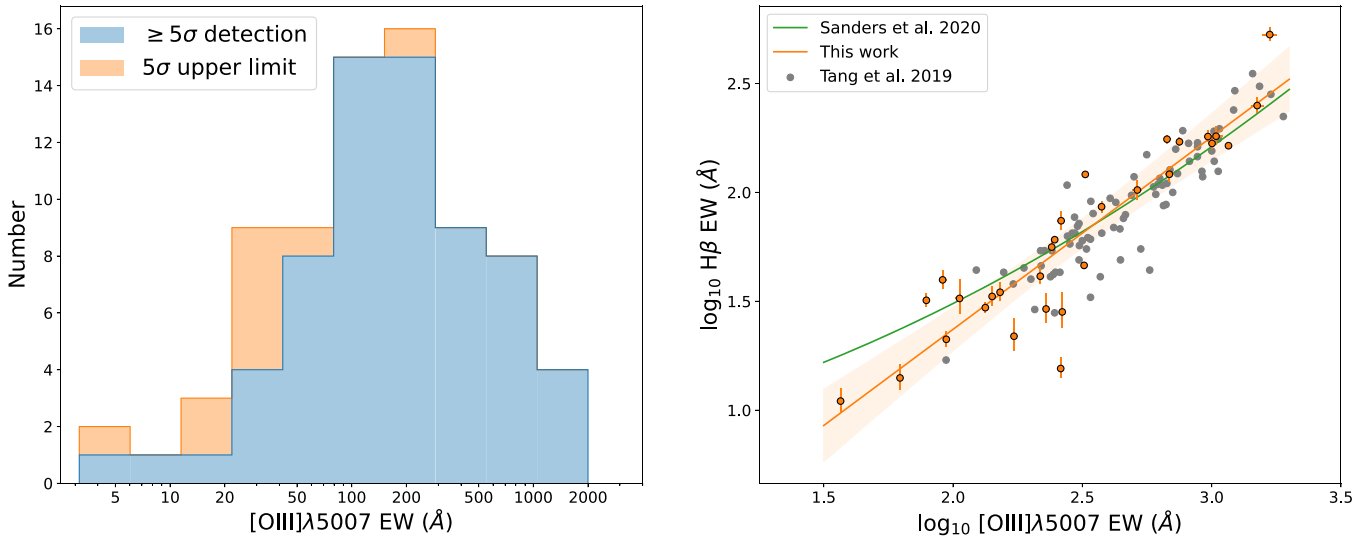
Figure 3. Rest-optical EW properties of $1 < z < 3.4$ SFGs. Left: the [O III]λ5007 rest-frame EW distribution of galaxies with NIRISS-detected ($\geqslant 5\sigma$) line emission. Stacked histograms show $\geqslant 5\sigma$ EW measurements (blue) and 5σ upper limits (orange), divided between 10 bins of equal logarithmic width. Right: the comparison of Hβ and [O III]λ5007 EWs, restricted to objects where both have $\geqslant 5\sigma$ measurements (in orange). We report a positive trend, in agreement with the overlaid $z \sim 2$ galaxy sample presented by Tang et al. (2021b, 2022; in gray). We also overlay the best-fit curve (green) for the $z \sim 2.3$ Sanders et al. (2020) sample, who utilize a second-order polynomial function. We use a linear function to model our data, which are shown in orange accompanied by the 2σ uncertainty for our data.

Table 1
Rest-optical Emission Line EWs for the $1.7 < z < 2.4$ (Where All Lines Are Observable) NIRISS-detected Sources

ID (NIRISS) (1)	R.A. (deg) (2)	Decl. (deg) (3)	z (NIRISS) (4, 5, 6)	Hα EW (Å) (7, 8)	[O III] EW (Å) (9, 10)	Hβ EW (Å) (11, 12)	[O II] EW (Å) (13, 14)
1911	3.586765	−30.390825	$2.213^{+0.001}_{-0.003}$	80.37 ± 4.77	70.56 ± 3.54	<8.13	24.95 ± 3.78
2205	3.586972	−30.387021	$1.864^{+0.001}_{-0.001}$	230.41 ± 12.12	305.21 ± 8.46	29.16 ± 4.50	<28.36
1208	3.576590	−30.399050	$1.872^{+0.001}_{-0.001}$	249.00 ± 8.08	500.33 ± 13.71	85.95 ± 5.35	45.07 ± 4.18
2707	3.585922	−30.380683	$1.862^{+0.001}_{-0.001}$	980.57 ± 33.70	1337.72 ± 48.96	167.85 ± 9.36	106.76 ± 8.94
1426	3.597289	−30.396712	$1.898^{+0.007}_{-0.002}$	<123.42	149.15 ± 17.34	<62.31	<68.84
951	3.583265	−30.403339	$1.894^{+0.003}_{-0.002}$	212.63 ± 21.71	109.76 ± 12.03	<51.88	81.09
950	3.582530	−30.402313	$1.895^{+0.002}_{-0.001}$	<94.77	211.30 ± 10.08	<40.78	<111.51
2616	3.591120	−30.381703	$1.885^{+0.001}_{-0.001}$	$<287.23 \pm 3.51$	428.25 ± 4.65	46.24 ± 1.71	41.77 ± 2.04
320	3.586433	−30.409363	$2.021^{+0.001}_{-0.001}$	772.55 ± 19.82	1001.00 ± 26.51	170.83 ± 7.23	56.85 ± 3.89
1002	3.598541	−30.401792	$2.012^{+0.001}_{-0.001}$	870.69 ± 25.02	895.90 ± 26.63	175.48 ± 8.22	53.87 ± 4.53
451	3.594058	−30.407999	$2.018^{+0.001}_{-0.001}$	2631.01 ± 145.88	2235.78 ± 140.12	530.46 ± 36.99	142.72 ± 9.48
1352	3.604190	−30.397187	$2.068^{+0.001}_{-0.001}$	163.38 ± 4.50	105.14 ± 2.80	31.96 ± 2.24	34.00 ± 2.59
2289	3.579076	−30.385963	$2.194^{+0.001}_{-0.001}$	607.38 ± 28.01	688.04 ± 27.85	102.58 ± 10.39	70.52 ± 8.02
1886	3.603156	−30.391074	$2.178^{+0.001}_{-0.001}$	601.62 ± 24.57	915.38 ± 35.40	121.17 ± 9.82	57.73 ± 5.88
2139	3.580030	−30.387832	$2.329^{+0.001}_{-0.001}$	218.86 ± 4.02	347.69 ± 4.43	15.54 ± 1.70	97.50 ± 2.66

Note. The columns provided in the machine-readable table for the full $1 < z < 3.4$ sample match those given here. Column (1) lists the IDs of the sources; (2) and (3) show the (J2000) R.A. and decl.; (4), (5), (6) report the `Grizli` maximum probability function redshift and the 16th and 84th redshift percentiles; the rest-frame equivalent width (EW) and uncertainty are given for the Hα, [O III], Hβ, and [O II] lines in columns (7)–(14). When 5σ EW upper limits are required, the EW_err is set to -99.

ionizing photons (e.g., Nakajima et al. 2020). These systems with large EWs are associated with very young stellar populations ($\lesssim 10$ Myr, e.g., Tang et al. 2021a), created during a recent burst of star formation, where the massive O/B-type stars responsible for the production of the high-energy ionizing UV photon required to produce doubly ionized oxygen still remain in the population. We note that EW thresholds based on hydrogen recombination lines can be theoretically motivated from population syntheses of a stellar population at a given age (e.g, Dottori 1981; Leitherer et al. 1999) and are largely insensitive to star formation history (SFH) and metallicity;

however, it is still common to choose to use the [O III] line because it allows studies to probe higher-redshift samples compared to Hα, and is typically the strongest rest-optical emission line (e.g., compared to Hβ), which reduces the uncertainty in EW measurements.

We find that out of the 76 initial targets with NIRISS line detections, 12% (9/76) are considered EELGs according to our threshold. This value is larger than the measured rate (3.8% >750 Å) at $z \sim 2$ from Boyett et al. (2022), who utilize HST/ WFC3 WFSS. We note that these two values may differ due to the sample selection, given that the quality of the

NIRISS/WFSS allows us to extract spectra from sources up to 2 mag fainter (at $\lambda \sim 1.5\ \mu$m) and Boyett et al. (2022) employ an M_{UV} restriction. Additionally, the requirement for our sample to have a spectroscopic redshift based on previous line detections may bias our sample toward stronger line emitters, although we may also miss extreme line emitters with faint continua, due to the requirement of a detection in our direct imaging. Future work will consider the completeness in detail.

Our NIRISS/WFSS sample allows us to study the characteristics of these SFGs. The Hβ EW is shown to be a good indicator of the age of a stellar population (e.g., Flury et al. 2022a, 2022b) and in this sample we determine a strong relation between the [O III]λ5007 and Hβ EW. This supports the theory that very young stars are required in our large-EW SFGs to produce the high-energy photons needed for the production of doubly ionized oxygen.

The identification of the extreme EW population in our analysis selects a sample of efficient ionizing agents. However, this selection will not contain all UV-ionizing sources. Extremely metal-poor galaxies can exhibit the characteristics we have ascribed to EELGs without exhibiting extreme [O III] λ5007 EWs, as has been seen in local extremely metal-poor dwarf galaxies (e.g., Izotov et al. 2001, 2021). Evidence for galaxies with young stellar populations but low [O III] EW has also been recently reported at $z > 7$ by Endsley et al. (2022), which has also been attributed to very low metallicity or a large escape fraction of ionizing photons. Therefore, the fraction of SFGs that are EELGs provides a lower threshold to the true abundance of efficient ionizing agents within the SFG population; further work into the dependence of [O III] emission on metallicity and escape fraction is needed to determine the abundance of the low-[O III] EW ionizing sources. We have provided a first study of the rest-optical properties of EELGs based on NIRISS observations, and to higher redshifts than achievable with HST/WFC3 WFSS. We await upcoming JWST/NIRISS programs, including, CANUCS [GTO 1208, PI Willott] and PASSAGE [GO 1571, PI Malkan], to provide greater statistical analysis through large area surveys (involving multiple NIRISS pointings).

6. Conclusions

The GLASS-ERS program provides some of the earliest and deepest JWST extragalactic observations, and in this Letter we have used deep NIRISS/WFSS to study $1 < z < 3.4$ SFGs in the A2744 region. From our initial spectroscopic sample of galaxies, we detect line emission in 89% (76/85) of targets with extracted spectra. We find good agreement in the spectroscopic redshift measurements from NIRISS and previous ground- and space-based studies, confirming the redshift of 74 objects and with only 2 objects identified using NIRISS to have an alternative redshift to their previous values. We note there is still subtle differences in the spectroscopic redshifts with 14% of the sample (11/76 objects) having a change in measurement greater than $\geqslant 5\sigma_{NMAD}$ where $\sigma_{NMAD} = 0.003$. We caution that visual inspection was required in a significant fraction of cases (23/76) to clearly identify the emission lines. This will likely improve with updates to contamination modeling and NIRISS calibrations.

We determine the observed rest-frame [O III]λ5007 EW distribution, ranging from $\sim$10–2000 Å, with a turnover at $\sim$150 Å. We identify an EELG subsample of nine (12%) galaxies with EW $\geqslant$750 Å, an abundance higher than what was found in previous studies. This discrepancy likely arises from the inherent incompleteness of our sample due to the preselection of spectroscopically identified sources and our line sensitivity, although we note the sensitivity of NIRISS allows our sample to include extracted spectra from galaxies up to 2 mag fainter in the near-infrared and to higher redshift than previous HST/WFSS studies. Finally, we find a correlation between the [O III]λ5007 and Hβ EWs, supporting the theory that very young stellar populations are required to produce the high-energy photons needed to produce [O III].

This study provides a first demonstration of the capabilities of JWST/NIRISS for studying rest-optical emission lines in high-redshift SFGs. We anticipate that future studies of SFG spectra through NIRISS/WFSS will advance greatly over the first cycles of JWST science, as planned wide area surveys including PASSAGE and CANUCS unlock large galaxy samples, allowing statistical analysis of the rare EELG population.

Data Availability

We provide measured rest-optical emission line properties (Table 1) for the full sample in a machine-readable format. Further catalogs and the routines used in this work are available from the authors upon reasonable request. The raw JWST observations are publicly available from STSCI and on MAST at doi:10.17909/s6nb-x394.

ORCID iDs

K. Boyett (ID) https://orcid.org/0000-0003-4109-304X
S. Mascia (ID) https://orcid.org/0000-0002-9572-7813
L. Pentericci (ID) https://orcid.org/0000-0001-8940-6768
N. Leethochawalit (ID) https://orcid.org/0000-0003-4570-3159
M. Trenti (ID) https://orcid.org/0000-0001-9391-305X
G. Brammer (ID) https://orcid.org/0000-0003-2680-005X
G. Roberts-Borsani (ID) https://orcid.org/0000-0002-4140-1367
V. Strait (ID) https://orcid.org/0000-0002-6338-7295
T. Treu (ID) https://orcid.org/0000-0002-8460-0390
M. Bradac (ID) https://orcid.org/0000-0001-5984-0395
K. Glazebrook (ID) https://orcid.org/0000-0002-3254-9044
A. Acebron (ID) https://orcid.org/0000-0003-3108-9039
P. Bergamini (ID) https://orcid.org/0000-0003-1383-9414
A. Calabrò (ID) https://orcid.org/0000-0003-2536-1614

M. Castellano https://orcid.org/0000-0001-9875-8263

A. Fontana https://orcid.org/0000-0003-3820-2823

C. Grillo https://orcid.org/0000-0002-5926-7143

A. Henry https://orcid.org/0000-0002-6586-4446

T. Jones https://orcid.org/0000-0001-5860-3419

D. Marchesini https://orcid.org/0000-0001-9002-3502

C. Mason https://orcid.org/0000-0002-3407-1785

A. Mercurio https://orcid.org/0000-0001-9261-7849

T. Morishita https://orcid.org/0000-0002-8512-1404

T. Nanayakkara https://orcid.org/0000-0003-2804-0648

P. Rosati https://orcid.org/0000-0002-6813-0632

C. Scarlata https://orcid.org/0000-0002-9136-8876

E. Vanzella https://orcid.org/0000-0002-5057-135X

B. Vulcani https://orcid.org/0000-0003-0980-1499

X. Wang https://orcid.org/0000-0002-9373-3865

C. Willott https://orcid.org/0000-0002-4201-7367

References

Amorin, R., Perez-Montero, E., Contini, T., et al. 2015, A&A, 578, A105

Atek, H., Kneib, J. -P., Pacifici, C., et al. 2014, ApJ, 789, 96

Atek, H., Malkan, M., McCarthy, P., et al. 2010, ApJ, 723, 104

Atek, H., Siana, B., Scarlata, C., et al. 2011, ApJ, 743, 121

Bagley, M. B., Scarlata, C., Mehta, V., et al. 2020, ApJ, 897, 98

Bergamini, P., Acebron, A., Grillo, C., et al. 2022, arXiv:2207.09416

Boyett, K. N. K., Stark, D. P., Bunker, A. J., Tang, M., & Maseda, M. V. 2022, MNRAS, 513, 4451

Brammer, G., & Matharu, J. 2021, gbrammer/grizli: Release 2021 v1.3.2, Zenodo, doi:10.5281/zenodo.1146904

Brammer, G. B., van Dokkum, P. G., & Coppi, P. 2008, ApJ, 686, 1503

Dottori, H. A. 1981, Ap&SS, 80, 267

Doyon, R., Hutchings, J. B., Beaulieu, M., et al. 2012, Proc. SPIE, 8442, 84422R

Du, X., Shapley, A. E., Tang, M., et al. 2020, ApJ, 890, 65

Endsley, R., Stark, D. P., Chevallard, J., & Charlot, S. 2021, MNRAS, 500, 5229

Endsley, R., Stark, D. P., Whitler, L., et al. 2022, arXiv:2208.14999

Flury, S. R., Jaskot, A. E., Ferguson, H. C., et al. 2022a, ApJS, 260, 1

Flury, S. R., Jaskot, A. E., Ferguson, H. C., et al. 2022b, ApJ, 930, 126

Izotov, Y. I., Chaffee, F. H., Foltz, C. B., et al. 2001, ApJ, 560, 222

Izotov, Y. I., Thuan, T. X., & Guseva, N. G. 2021, MNRAS, 504, 3996

Leitherer, C., Schaerer, D., Goldader, J. D., et al. 1999, ApJS, 123, 3

Lotz, J. M., Koekemoer, A., Coe, D., et al. 2017, ApJ, 837, 97

Maseda, M. V., van der Wel, A., Rix, H.-W., et al. 2018, ApJ, 854, 29

Momcheva, I. G., Brammer, G. B., van Dokkum, P. G., et al. 2016, ApJS, 225, 27

Nakajima, K., Ellis, R. S., Robertson, B. E., Tang, M., & Stark, D. P. 2020, ApJ, 889, 161

Oke, J. B., & Gunn, J. E. 1983, ApJ, 266, 713

Onodera, M., Shimakawa, R., Suzuki, T. L., et al. 2020, ApJ, 904, 180

Richard, J., Claeyssens, A., Lagattuta, D., et al. 2021, A&A, 646, A83

Roberts-Borsani, G., Morishita, T., Treu, T., et al. 2022, ApJL, 938, L13

Sanders, R. L., Shapley, A. E., Reddy, N. A., et al. 2020, MNRAS, 491, 1427

Schmidt, K. B., Treu, T., Brammer, G. B., et al. 2014, ApJL, 782, L36

Smit, R., Bouwens, R. J., Labbe, I., et al. 2014, ApJ, 784, 58

Tang, M., Stark, D. P., Chevallard, J., et al. 2021a, MNRAS, 501, 3238

Tang, M., Stark, D. P., Chevallard, J., et al. 2021b, MNRAS, 503, 4105

Tang, M., Stark, D. P., Chevallard, J., & Charlot, S. 2019, MNRAS, 489, 2572

Tang, M., Stark, D. P., & Ellis, R. S. 2022, MNRAS, 513, 5211

Terlevich, R., Terlevich, E., Melnick, J., et al. 2015, MNRAS, 451, 3001

Treu, T., Roberts-Borsani, G., Bradac, M., et al. 2022, ApJ, 935, 110

Treu, T., Schmidt, K. B., Brammer, G. B., et al. 2015, ApJ, 812, 114

Vanzella, E., Castellano, M., Bergamini, P., et al. 2022, arXiv:2208.00520

van der Wel, A., Straughn, A. N., Rix, H. W., et al. 2011, ApJ, 742, 111

Wang, Xin, Jones, Tucker, Vulcani, Benedetta, et al. 2022, ApJL, 938, L16

Willott, C. J., Doyon, R., Albert, L., et al. 2022, PASP, 134, 025002